



Oxygen vacancy enhanced visible light photocatalytic selective oxidation of benzylamine over ultrathin Pd/BiOCl nanosheets

Shuai Wei^a, Hongxiao Zhong^a, Hongtao Wang^a, Yujie Song^{a,b,*}, Chunman Jia^a, Masakazu Anpo^{b,c}, Ling Wu^{b,**}

^a Hainan Provincial Key Laboratory of Fine Chemicals, Hainan University, Haikou 570228, PR China

^b State Key Laboratory of Photocatalysis on Energy and Environment, Fuzhou University, Fuzhou 350116, PR China

^c Department of Applied Chemistry Graduate School of Engineering, Osaka Prefecture University, Osaka 599-8531, Japan

ARTICLE INFO

Keywords:

Two atom layered BiOCl nanosheets
Oxygen vacancy
Interface coordination
Visible light photocatalysis
Selective oxidation of benzylamine

ABSTRACT

Two atomic layered BiOCl nanosheets with rich oxygen vacancies (NS-OV) were constructed via surface Pd deposition (0.5 wt%) as a multifunctional photocatalyst (Pd_{0.5}/NS-OV), which exhibits high conversion (>95%) and precise selectivity (>98%) for benzylamine coupling to N-benzylidenebenzylamine under visible light irradiation and 1 atm air pressure. XPS and UV-vis DRS indicated that ultrathin structure of the nanosheets induces the formation of surface oxygen vacancies (OV), resulting in abundant surface low-coordinated Bi atoms and expanded visible light absorption. Moreover, in-situ EPR results revealed that surface OV sites contribute to assemble O₂ molecules from air to surface of NS-OV. Additionally, in-situ FTIR suggested that low-coordinated Bi selectively adsorb benzylamine molecules via -N...Bi- coordination bonds at the interfaces, inducing polarization and activation of -C-N bonds. Furthermore, Pd sites were observed to crucially participate in formation of active •O₂⁻ species under visible light irradiation. Based on multifunctional features, a possible synergistic mechanism was proposed.

1. Introduction

Photocatalytic organic transformation to produce useful compounds with a green and sustainable process has been given much attention, especially, in the relation to the industrial production in environmentally friendly and sustainably economical way [1–3]. Various imines are multifunctional intermediates for the synthesis of pharmaceuticals, bioactive compounds and fine chemicals. Therefore, photocatalytic synthesis of imines is strongly desired to their high research values as a hotspot [4–6]. In the last decades, various kinds of photocatalysts have been developed for the selective catalytic oxidation of benzylamine to its corresponding imines under the mild conditions at room temperature and 1 atm O₂ pressure, using such as BiVO₄ [7], WO₃ [8], TiO₂ [9], g-C₃N₄ [10,11], COFs [12,13], MIL-125 [14], and PCN822 [15]. These studies have greatly promoted the development of photocatalytic synthesis of imines, especially, even under visible light irradiation.

Furthermore, more and more researches have focused on the fundamental chemistry of the surface/interface in heterogeneous

photocatalysis based on the physical chemistry methods [16,17]. For example, the chemical adsorption of reactant molecules was found to lead the high catalytic activity through the formation of surface coordination bonds [18,19]. Thus, the construction of photocatalyst with the special surface functional sites for the selective chemical adsorption and activation of benzylamine is strongly desired. In addition, a visible light-driven photocatalytic system for this reaction is also important to overcome the demands for pure O₂.

Two-dimensional (2D) nanosheets have been widely applied as photocatalysts in various fields due to their high ability in the separation of the electron-holes, their available high surface areas and also their high exposure of the surface functional sites [20–25]. These characteristic features of 2D nanosheets play an important role in the chemical adsorption of the reactant molecules on the surface/interface. Moreover, the ultrathin 2D structure with a few atoms thickness provides an ideal model to deeply investigate the surface adsorption, coordination and transformation processes at a molecules level.

Many ultrathin nanosheets such as WO₃ [8], few-layer C₃N₄ [10], 2D

* Corresponding author at: Hainan Provincial Key Laboratory of Fine Chemicals, Hainan University, Haikou 570228, PR China.

** Corresponding author.

E-mail addresses: songyujie@hainanu.edu.cn (Y. Song), wuling@fzu.edu.cn (L. Wu).

porphyrin-based COF [26] have been reported in photocatalytic oxidation of benzylamine to imines, suggesting the potential values of these ultrathin nanosheets photocatalysts. Some of them focused more attention on the surface/interface interactions behaviors of benzylamine in the photocatalytic reactions. As a new type of photocatalysts, Bismuth oxychloride (BiOCl) have been given much attentions [27–29]. BiOCl has a layered structure composed by the alternately accumulated $[\text{Bi}_2\text{O}_2]^{2+}$ layer and double $[\text{Cl}]^-$ layers along the (001) direction [30]. The two adjacent lamella of BiOX are connected by a non-covalent promoting. In particular, the monolayer BiOCl nanosheets are expected to have more surface metals with coordinatively unsaturated sites, vacancies and dangling bonds [31]. The coordinatively unsaturated surface Bi^{3+} sites exhibit a strong Lewis acidic property, leading to the selective adsorption and activation of the reactant molecules via the chemical coordination on interface, resulting in an enhancement of photocatalytic activities [32,33].

Furthermore, the oxygen vacancies (OV) are easily formed as the (001) face of BiOCl nanosheets [34,35]. The surface OV sites play an important role not only in the extension of the photoresponse and improving the surface conductivity but also in operating as electron donors and adsorption sites for O_2 to result in the production of active oxygen species [36,37]. Thus, the precise fabrication of surface OV in BiOCl nanosheets is important to achieve a visible light-driven photocatalytic oxidation of benzylamine to form imines at 1 atm air pressure and room temperature. Furthermore, the deep insight into the functions of the surface OV sites as well as the Lewis acidic sites are important to achieve a high selective adsorption of the reactants with a high molecule recognition feature and efficient transformation into the products on the surface/interface of monolayer BiOCl nanosheets.

In the context of these circumstances, we have designed a functional photocatalyst composed by the monolayer BiOCl nanosheets with the rich oxygen vacancies (NS-OV) and 0.5% (wt) Pd nanoparticles in aiming to the oxidative coupling of benzylamine. The obtained results show the highly efficient transformation of benzylamines to its corresponding imines under visible light irradiation at 1 atm air pressure and room temperature. The crystal phases, morphologies, surface chemical states and electronic structure of the photocatalyst are fully characterized and analyzed by using XRD, SEM, TEM, AFM, XPS and EPR techniques. Moreover, in-situ FTIR clearly exhibit the selective adsorption of the reactant with molecular recognition and the interface electrons polarization of benzylamine molecules on the surface low-coordinated Bi sites through the formation of the coordination bonds of $-\text{N}\cdots\text{Bi}-\text{O}$. Also, the in-situ EPR results clearly indicate that the adsorption, concentration and activation of O_2 molecules to produce active $\cdot\text{O}_2^-$ anion species proceed under assistance of the surface OV sites. The role of Pd nanoparticles in the hydrogen transfer from benzylamine is also clarified. Based on these experimental results, a possible reaction mechanism is proposed for the photocatalytic oxidative coupling of benzylamine into N-benzylidenbenzylamine on the ultrathin Pd/BiOCl nanosheet catalysts.

2. Experimental section

2.1. Reagents and chemicals

NaCl was purchased from Xilong Chemical Co., Ltd, Mannitol, Polyvinylpyrrolidone (PVP), Bismuth (III) nitrate pentahydrate ($\text{Bi}(\text{NO}_3)_3 \cdot 5\text{H}_2\text{O}$), Acetonitrile, Benzylamine and N-Benzylidenbenzylamine were purchased from Beijing Innochem Science & Technology co., LTD. All the reagents were analytical grade and used without further purification.

2.2. Photocatalyst preparation

2.2.1. Synthesis of the ultrathin BiOCl nanosheets photocatalysts

The ultrathin BiOCl nanosheets with the oxygen vacancies (denoted

as NS-OV) were synthesized via improving the previously reported method [30,33]. Firstly, 0.8 g PVP and 2 mmol $\text{Bi}(\text{NO}_3)_3 \cdot 5\text{H}_2\text{O}$ were dissolved in 50 mL mannitol solution (0.1 M) and stirred vigorously for 15 min. Then, 10 mL of saturated sodium chloride solution was slowly added into the mixture with stirring. The mixture was continuously stirred for 10 min and transferred into a 100 mL Teflon-lined stainless steel autoclave. After the reaction for 5 h at 160 °C, the precipitates were separated via centrifugation. The obtained products were washed with deionized water and ethanol several times to remove the residual ions. Finally, the products were dried at 60 °C for 12 h.

For comparison, BiOCl nanoplates with less oxygen vacancies (denoted as Plate) were also prepared by the same procedures. However, the PVP was absent in this procedures. Moreover, a bulk BiOCl free of oxygen vacancies sample (denoted as Bulk) was also prepared via the above mentioned hydrothermal method. But, PVP and mannitol were not added.

2.2.2. Surface Pd nanoparticles construction on the NS-OV

The NS-OV was constructed on the surface by an in situ photo-deposition of Pd nanoparticles (Pd/NS-OV). 50 mg of the prepared NS-OV powder was dispersed in the mixed solution of 20 mL deionized water and 5 mL methanol. The test of the reaction was carried out in the conditions of the completely replaced air by N_2 under stirring and maintaining in N_2 atmosphere. Then, a certain volume of palladium nitrate solution (0.05 M) was added in the mixed solution. Under 1 h irradiation with a Xe lamp, the precipitates were collected by centrifugation and washed by deionized water. The obtained products were dried at 60 °C for 12 h. Moreover, the contents of the loaded Pd nanoparticles on the surfaces were also regulated by controlling the added volume of $\text{Pd}(\text{NO}_3)_2$ solution. 0.25% (wt), 0.5% (wt), 0.75% (wt) and 1% (wt) Pd supported catalysts were denoted as $\text{Pd}_{0.5}/\text{NS-OV}$, $\text{Pd}_{0.25}/\text{NS-OV}$, $\text{Pd}_{0.75}/\text{NS-OV}$ $\text{Pd}_1/\text{NS-OV}$, respectively.

2.3. Materials characterization

The X-ray diffraction (XRD) of the prepared catalysts were measured on the Rigaku SmartLab with $\text{Cu K}\alpha$ radiation using 40 kV working voltage and 30 mA working current. The morphology of the catalyst was observed by a scanning electron microscope (SEM) on Hitachi S-4800 electron microscope. Transmission electron microscopy (TEM) and higher-resolution transmission electron microscopy (HRTEM) images were obtained by FEI Talos F200X microscope with 200 kV accelerating voltage. The thickness of the synthesized nanosheets was measured by an atomic force microscope (AFM). The UV–vis diffuse reflectance spectra (DRS) of the catalysts were obtained by a UV–vis spectrophotometer (UV-2600). The Fourier transform infrared (FT-IR) spectra were recorded on a spectrometer (Thermo Nicolet i550). X-ray photoelectron spectra (XPS) were carried on a Thermo Escalab 250Xi XPS system with $\text{Al K}\alpha$ as the excitation source and the reference C1s binding energy was 284.8 eV. Electron paramagnetic resonance (EPR) signals were recorded on a JES FA200 spectrometer at room temperature using a 300 W Xe lamp as light source (Beijing Trustech, PLS-SXE300D) with a 400 nm cutoff filter.

2.4. In-situ FTIR measurements

The in-situ FTIR analysis of benzylamine (BA) and N-benzylidenbenzylamine adsorbed on the catalysts was measured by Fourier transform infrared spectrometer (NICOLET i550) with a resolution of 4 cm^{-1} and 64 scans of each spectrum. First, the 20 mg catalyst was pressed into a self-supporting infrared disk, and then the disk was fixed on the sample rack, which was moved vertically along the glass tube. Before measuring the spectrum, the catalyst was treated in dynamic vacuum conditions (5×10^{-2} hPa) for 3 h at 150 °C to remove surface contaminants. The Fourier transform infrared spectra of the catalysts were measured after the disks were cooled to room temperature. 20 μL BA or N-

benzylidenbenzylamine was then injected into the glass tube with a syringe. After reaching to the adsorption equilibrium for 30 min, Fourier transform infrared spectroscopy was collected to study the physical and chemical features of the adsorption of BA/N-benzylidenbenzylamine on the catalyst. The physically weakly adsorbed BA/N-benzylidenbenzylamine was removed by the evacuation of the cell for 15 min at 150 °C under the vacuum of 5×10^{-2} hPa. Finally, Fourier transform infrared spectroscopy was also collected to study the chemisorption of BA and N-benzylidenbenzylamine molecules on the catalyst.

2.5. Electrochemistry measurements

Electrochemical measurements were recorded in the electrochemical workstation (IVIUM-N-STAT) with 0.2 M Na₂SO₄ solution as an electrolyte. The pH value of the solution is measured by a pH meter as about 6.8. The standard three electrode system was used for measurements, using FTO glass coated with catalyst, saturated Ag/AgCl electrode and Pt foil as working electrode, reference electrode and counter electrode, respectively. The Mott-Schottky analysis, electrochemical impedance spectroscopy (EIS) measurements and photocurrent response measurements were performed at the electrochemical workstation.

2.6. Photocatalytic oxidative coupling of benzylamine

The mixture of 10 mg catalyst, 0.2 mmol BA and acetonitrile of 1.5 mL were added into a 15 mL Pyrex glass reaction tube at 1 atm air pressure. Then, under stirring, the suspension was irradiated using a 300 W Xe lamp equipped with a 400 nm-cutoff filter. The optical power density of the used Xe lamp have been measured by a light intensity meter as about 1.1 W cm^{-2} . After irradiation for 12 h at room temperature of 25 °C, the mixtures were centrifuged, and the supernatants were filtered with a high molecular membrane syringe. The amounts of the reactants and products were analyzed by gas chromatography (Shimadzu GC-2014 C) with a RTX-5 chromatographic column (Fig. S1). The temperatures of the injector and detector are maintained at 280 °C. The pressure of injection is set as 88.9 KPa. Column temperature program is programmed from 80 °C holding 2 min to 280 °C holding 5 min at 20 °C/min. The injection volume was 1 µL. Gas chromatography-mass spectrometry (GC-MS) was carried out to confirm the products on GC-MS QP 2010. The standard curves of the BA (Fig. S2a) and N-benzylidenbenzylamine (Fig. S2b) are obtained to calculate the conversion of BA and the selectivity for the formation of N-benzylidenbenzylamine. Defined as follows:

$$\text{Conversion (\%)} = [(C_0 - C_{BA})/C_0] \times 100$$

$$\text{Selectivity (\%)} = [C_{\text{N-benzylidenbenzylamine}} \times 2/(C_0 - C_{BA})] \times 100$$

Where C_0 is the initial amount of BA, C_{BA} and $C_{\text{N-benzylidenbenzylamine}}$ are the amounts of the substrate BA and its corresponding product of N-benzylidenbenzylamine, respectively.

3. Results and discussion

3.1. Characterization of the prepared samples

The crystal structures of the prepared catalysts were characterized by XRD. As shown in Figs. S3 and S4, the single-phase diffraction patterns are matched well with the standard card of BiOCl crystal (JCPDS # 6-0249) [38]. The surface construction of Pd scarcely causes any changes in the crystal structure of NS-OV. Moreover, the peaks due to Pd is not observed for the Pd_{0.5}/NS-OV, which being attributed to the small size of Pd nanoparticles and their highly dispersion [39]. Compared with the Plate catalyst, the NS-OV exhibits a wider half peak, indicating that the utilization of PVP is critical to form a preferred orientation. The NS-OV catalyst preferred to grow along the (110) direction, exhibits a

reduction in the thickness of building units and the formation of ultrathin structure [40]. The morphological characteristics of the prepared catalyst were characterized by SEM. As shown in Fig. 1a, the Plate catalyst shows a cubic block structure. Obviously, as shown in Fig. 1b, the NS-OV exhibits a thin sheet structure. Moreover, the Bulk catalyst has an irregular shape and thickness (Fig. S5). These results are consistent with the results obtained by XRD measurements. Furthermore, the TEM images have also confirmed the ultrathin structure of the NS-OV catalyst. Fig. 2a shows the TEM image of the transparent nanosheet of NS-OV with Pd nanoparticles loaded on surface. As shown in Fig. 2b, the HRTEM images of the catalyst show the lattice stripes of 0.225 nm assigned to the (111) plane of cubic Pd and 0.275 nm assigned to (110) plane of BiOCl, respectively. The EDS (Fig. S6) also proves the introduction of Pd element. Moreover, as shown in Fig. 2c-d, the HAADF image and mapping also exhibits that the Pd nanoparticles are highly dispersed on the NS-OV. The content of Pd in the Pd_{0.5}/NS-OV was determined using inductively coupled plasma optical emission spectrometry (ICP-OES). The actual content of Pd was 0.49% (wt), being consistent with the calculated value. These results clearly demonstrate that the Pd_{0.5}/NS-OV composite has been successfully fabricated. The thickness of the prepared NS-OV was measured by AFM. As shown in Fig. 3a-b, the average thickness of the NS-OV is about 1.5 nm. It has been reported that the c parameter of BiOCl is 0.737 nm [30]. Therefore, these results suggest that the obtained NS-OV has a thickness of 1.5 nm consisting of 2 [Cl-Bi-O-Bi-Cl] units. Thus, the ultrathin NS-OV with two atomic layered thickness has been successfully obtained.

X-ray photoelectron spectroscopy (XPS) was conducted to further investigate the chemical states of the surface atoms on the prepared catalysts. Fig. 4a exhibits the XPS spectra of the NS-OV and Pd_{0.5}/NS-OV. The peaks attributed to Bi, O, Cl and C elements have been completely confirmed for both catalysts. On the other hand, the signal peaks due to Pd element in the Pd_{0.5}/NS-OV is not observed since its content is too low for the detection. As shown in Fig. 4b, the high resolution spectrum for Pd 3d in the Pd_{0.5}/NS-OV catalyst exhibits a pair of spin-orbit doublet of Pd 3d_{5/2} and Pd 3d_{3/2} with the binding energy of 335.04 and 340.17 eV, respectively, corresponding to Pd⁰ (metallic palladium) [41]. Moreover, in the high resolution spectra of Bi 4f shown in Fig. 4c, the peaks at binding energy of 158.93 and 164.23 eV attributable to the Bi³⁺ 4f_{7/2} and 4f_{5/2}, respectively, suggest the presence of Bi³⁺ sites on the surfaces of NS-OV. The positions of a peak of Bi³⁺ 4f in Pd_{0.5}/NS-OV shifts to the higher binding energy to be 159.10 and 164.4 eV, respectively. Similarly, as shown in Fig. 4d, the peaks of Cl 2p in Pd_{0.5}/NS-OV exhibit the higher binding energy than that of Cl 2p in NS-OV. These results clearly indicated that the introduction of Pd induces the assemblage of electrons to Pd atoms from Bi³⁺ on the surfaces via the interface connection [42–44]. These electron movement was found to result in the further formation of the surface Bi sites with coordination unsaturation.

Furthermore, the chemical states of the surface O has been studied to deeply understand the electronic features of catalytic function of the O sites. Fig. 4e exhibits the O1s spectra of NS-OV on a BiOCl plate (Plate) as for the reference. The asymmetric O1s peaks of NS-OV and Plate catalyst are deconvoluted into three different peaks, indicating the presence of different three types of O atoms on the surface of the prepared catalyst. These O species are classified into (i) lattice oxygen (O1), (ii) surface hydroxyl (O2) and (iii) adsorbed oxygen (O3) [45]. To further study the effect of structure on the formation of these oxygen surface species, the bulk BiOCl (Bulk) catalyst with much more layers than Plate and NS-OV catalysts was prepared. Fig. S7a indicates the surface elements of Bi, Cl and O in the Bulk catalyst, being consistent with these of the NS-OV. However, in the high resolution of O 1s spectrum (Fig. S7b), only two peaks are deconvoluted into 530.10 and 531.48 eV, suggesting the presence of two different kinds of surface oxygen species (O1 and O2) in the Bulk catalyst. The atomic percentages of each oxygen species (at%) are determined from the data for the NS-OV, Plate and Bulk catalyst, respectively, as listed in Table S1. The

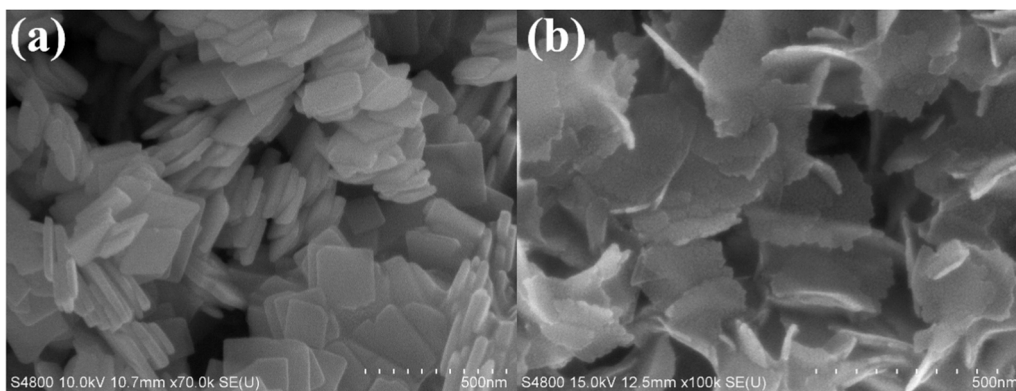


Fig. 1. SEM images of the prepared catalysts, (a) Plate and (b) NS-OV.

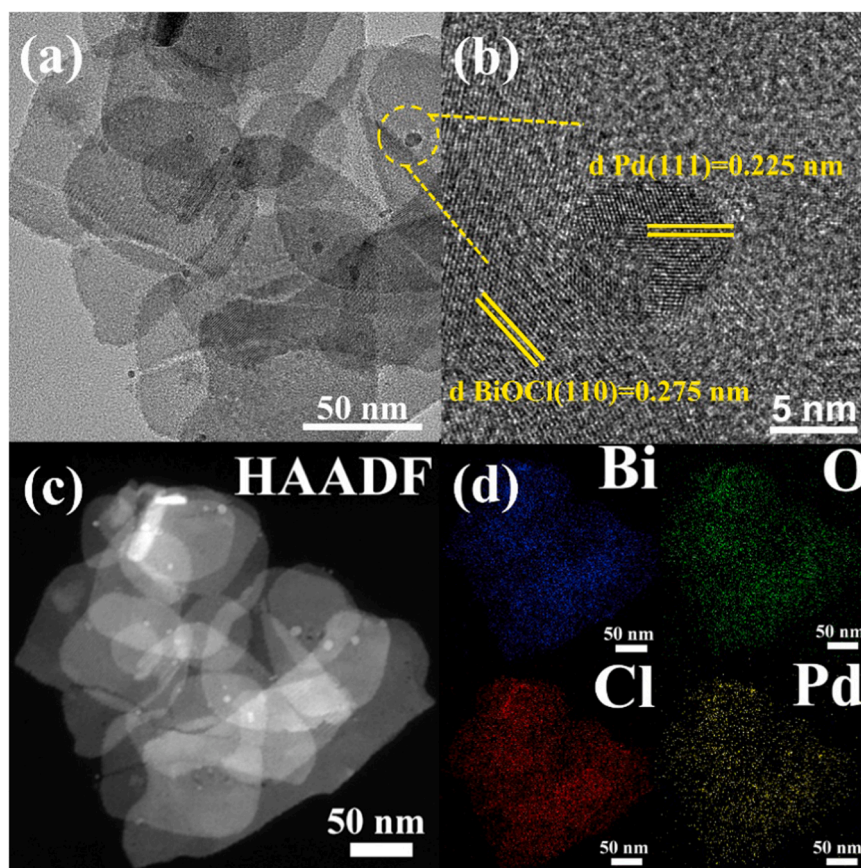


Fig. 2. TEM images of the $\text{Pd}_{0.5}/\text{NS-OV}$ (a-b), HAADF imaging and the corresponding elemental mappings of the $\text{Pd}_{0.5}/\text{NS-OV}$ catalyst (c-d).

proportion of the oxygen species adsorbed on the surface of NS-OV is about 21.21%, being higher than that in Plate (14.37%). Moreover, the ratio of the lattice oxygen in the NS-OV (50.51%) was found to be less than those in Plate (57.47%) and Bulk (75.76%). These results clearly indicated that much more oxygen vacancies (OV) were formed in the surface of NS-OV [46].

Thus generated surface OV sites were found to greatly enhance the amount of oxygen to the surface/interface of the NS-OV catalyst by providing oxygen from air. Furthermore, the surface OV sites were also found to enhance the coordination capacity of the metal Bi sites for the reactant molecules due to the appearance of the low-coordinated Bi sites on the surfaces. To confirm the presence of the OV sites in these catalysts, EPR spectra were measured. As shown in Fig. 4f, obvious ESP signals with a g value of 2.002 is observed for both the NS-OV and Plate

catalysts, clearly demonstrating the formation of unpaired electron species on these catalysts. This EPR signal is attributed to the oxygen vacancy [47]. In addition, as shown in Fig. 4f, the signal of the NS-OV exhibits higher intensity than that of the Plate, indicating that there are more OV sites on the NS-OV. On the other hand, the signal of OV unable to be detected in the EPR spectrum of Bulk catalyst (Fig. S8). These results clearly indicate the fact that the ultrathin BiOCl nanosheets with two atom layers thickness easily provide abundant available OV sites and also enhance the number of the surface metal sites coordinating to the interface for the surface/interface catalytic processes.

The energy band structure of a photocatalytic material is critical to determine the optical and electrical properties of the photocatalyst. Moreover, the surface OV sites have been reported to play an important role in determining the electronic structure of the photocatalyst [8,48,

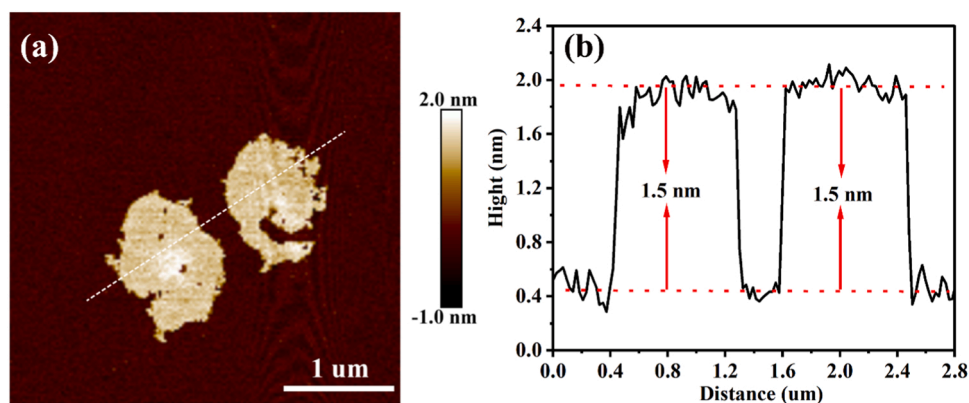


Fig. 3. AFM image (a) and the height profile image (b) of the prepared NS-OV catalyst.

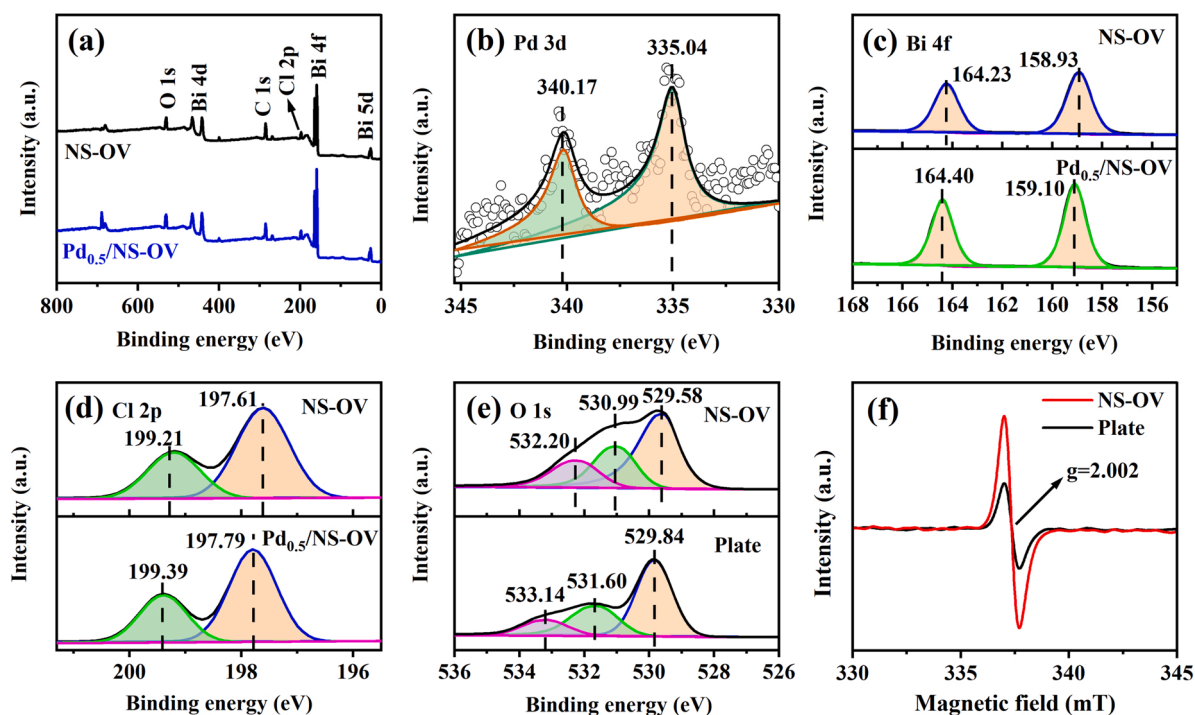


Fig. 4. (a) XPS survey of the NS-OV and $\text{Pd}_{0.5}/\text{NS-OV}$; (b) The high resolution spectrum for Pd 3d in $\text{Pd}_{0.5}/\text{NS-OV}$; (c-d) The high resolution spectra for Bi 4f, Cl 2p and O 1s in NS-OV and $\text{Pd}_{0.5}/\text{NS-OV}$, respectively; (e) The high resolution spectra for O1s in NS-OV and Plate, respectively; (f) EPR spectra for Plate and NS-OV.

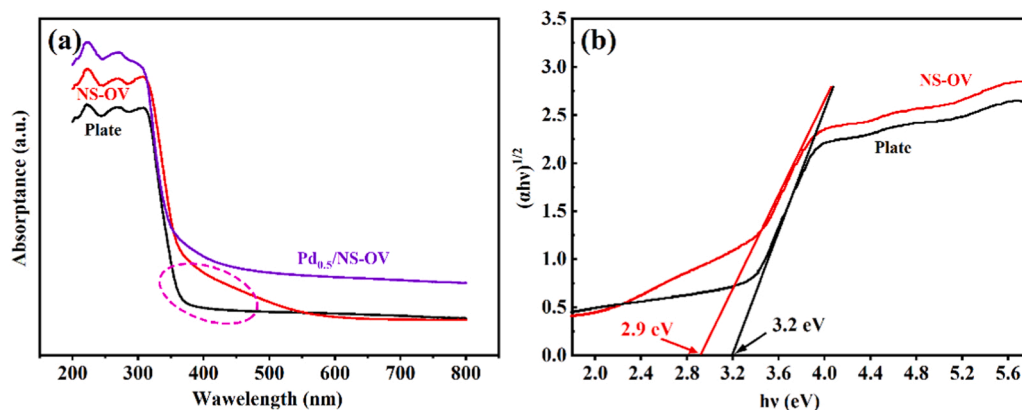


Fig. 5. (a) UV-vis DRS spectra and (b) Plot of $(\alpha hv)^{1/2}$ against $h\nu$ for the NS-OV and Plate.

49]. As shown in Fig. 5a, UV-vis DRS spectra of Plate and NS-OV exhibit the optical response from UV to visible light ranges with increasing the concentration of the surface OV sites. From the data (Fig. 5b), the band gap energy of Plate and NS-OV are estimated to be 2.90 eV and 3.20 eV, respectively. The photo-induced adsorption property of the NS-OV was enhanced by the deposition of Pd nanoparticles on the surfaces of the Pd_{0.5}/NS-OV, being attributed to the effect of Localized Surface Plasmon Resonance (LSPR). This effect has also been expected to facilitate the photocatalytic reactions [50].

As shown in Fig. S9a-b, the Mott-Schottky plots clearly exhibit the flat-band potential of NS-OV and Plate to be -1.25 V and -1.40 V, respectively, with Ag/AgCl as the counter electrode at pH 6.8, corresponding to -1.05 V and -1.20 V vs. NHE, respectively. These results clearly showed that the conduction band energy of these two catalysts are more negative than that of the O₂/•O₂⁻ (-0.28 V vs. NHE, Fig. S9c). Thus, O₂ molecules adsorbed on the surface of these catalysts are reduced to form the active •O₂⁻ anion radicals by the photo-generated electrons, contributing to the catalytic reactions [51]. By considering the band gap energies, the valence band energy levels (VB) of NS-OV and Plate were calculated to be 1.85 V and 2.00 V, respectively.

3.2. Performances of the prepared catalysts

The photocatalytic performance of the catalysts has been evaluated by selective photocatalytic oxidative coupling of benzylamine (BA) to form the desired corresponding product of N-benzylidenebenzylamine under visible light irradiation at room temperature and 1 atm air pressure. The results are listed in Table 1. As shown in Table 1, entry 1–3, the conversion of BA increases from 19.9% to 57.0% with increasing the concentration of the surface OV sites in Plate, Bulk and NS-OV. The conversion of BA is further improved by the addition of Pd nanoparticles (Table 1, entries 4–5). As shown in Table 1, entry 4, the Pd_{0.5}/NS-OV exhibits much higher photocatalytic conversion of BA (95.1%) with a high selectivity of 98.2% for the formation of N-benzylidenebenzylamine, being much better than those of Pd_{0.5}/Plate (entry 5). The NS-OV supported other metals, such as Pt_{0.5}/NS-OV and Cu_{0.5}/NS-OV, perform the less effective than the Pd_{0.5}/NS-OV (Table 1, entries 6–7). These results clearly indicate that Pd nanoparticles play an important role in an enhancement in the photocatalytic oxidation of BA on Pd_{0.5}/NS-OV. The turnover frequency (TOF) and turnover number (TON) of this reaction on the Pd_{0.5}/NS-OV catalyst were calculated to be 34.8 h⁻¹ and 410.4, respectively, using the moles of the converted benzylamine per hour and formed N-benzylidenebenzylamine per mole of Pd nanoparticles in the catalyst.

As shown in Table 1, entry 8 and 9, the products are not detected in the conditions without any photocatalysts nor under the dark condition. Furthermore, the photocatalytic BA transformation over the Pd_{0.5}/BiOCl

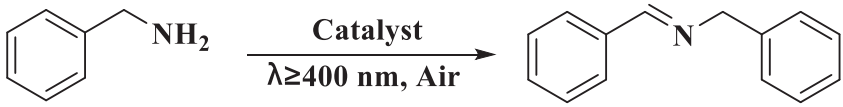
is explored under the irradiation of various light wavelength for 4 h with other conditions unchanged. As shown in Fig. S10, close to 100% conversion of BA with 76.3% selectivity of n-benzylidenebenzylamine is obtained over the Pd_{0.5}/NS-OV under the 320 nm wavelength of visible light irradiation. Moreover, the conversion of the BA is rapidly decreased to 41.5% with the increased selectivity of the n-benzylidenebenzylamine (98.9%) under the 400 nm wavelength of visible light irradiation. The conversion of BA sharply decreases to 6.5% conversion of BA with ~ 100% selectivity for n-benzylidenebenzylamine under the 450 nm wavelength of visible light irradiation. These results show that the reaction proceeds as a photocatalytic reaction under visible light irradiation (visible light-driven photocatalysis). In addition, as shown in Table 1, entry 10, only a trace of N-benzylidenebenzylamine is detected over the Pd_{0.5}/NS-OV when air is replaced with N₂. This result suggests that the presence of O₂ molecules is one of the critical requirements for the photocatalytic oxidative coupling of BA.

The effect of Pd-loaded on surfaces were explored by regulating the amount of Pd loadings. As shown in Fig. 6a, the photocatalytic conversion of BA first increases with increasing of the Pd nanoparticles from 0% to 0.5% (wt) and then decreases with continual increasing of the Pd to 1% (wt). On the other hand, the selectivity for the formation of N-benzylidenebenzylamine scarcely changes with changing the amount of surface Pd nanoparticles, revealing that the role of the surface Pd nanoparticles is only in promoting the conversion of BA. The excess Pd nanoparticles work to cover the functional surface sites of NS-OV, leading to the chemical adsorption of BA on the interfaces.

As shown in Fig. 6b, the relationship between the photocatalytic reaction features (conversion and selectivity) and the reaction time are fully investigated. The conversion of BA increases from 75% to 95.1% with expanding the reaction time from 8 h to 14 h, retaining the specific formation of N-benzylidenebenzylamine. However, the selectivity for the formation of the desired product exhibits to decrease after 12 h reaction, being attributed to the over oxidation of the product of N-benzylidenebenzylamine.

The solvent effect on the photocatalytic reaction has also been studied. As shown in Fig. S11, the high conversion of BA and high selectivity for the formation of N-benzylidenebenzylamine are observed in acetonitrile solvent (CH₃CN). Compared with acetonitrile (CH₃CN), the utilization of benzonitrile or toluene was found to decrease in the conversion of BA retaining the high selectivity for the formation of the desired product. These solvent effects are attributable to better dispersion of the photocatalyst in CH₃CN than in benzonitrile or toluene due to its large dielectric constant. Moreover, the Pd_{0.5}/NS-OV exhibited a poor accuracy for the formation of desired N-benzylidenebenzylamine in DMF and benzene solvents, being attributable to the polar diversity of these solvents due to their smaller dielectric constant. Thus, both reactant and product molecules are polarized depending on

Table 1
Photocatalytic oxidative coupling of benzylamine under visible light irradiation.^a

					
Entry	Catalyst	hν	Atm.	Conv. (%)	Sel. (%)
1	NS-OV	+	air	57.0	97.3
2	Plate	+	air	31.1	95.8
3	Bulk	+	air	19.9	93.1
4	Pd _{0.5} /NS-OV	+	air	95.1	98.2
5	Pd _{0.5} /Plate	+	air	43.4	93.0
6	Pt _{0.5} /NS-OV	+	air	85.9	90.7
7	Cu _{0.5} /NS-OV	+	air	40.1	88.9
8	Pd _{0.5} /NS-OV	-	air	0	0
9	-	+	air	0	0
10	Pd _{0.5} /NS-OV	+	N ₂	6.7	81.1

^a Reaction conditions: benzylamine (0.2 mmol), catalyst (10 mg), acetonitrile (1.5 mL), air (1 atm), irradiation time (12 h).

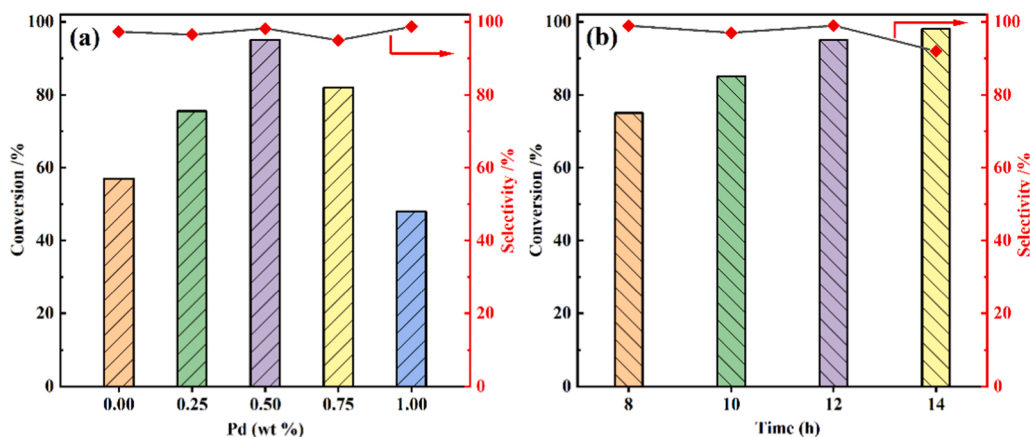


Fig. 6. The influences of the surface Pd loading on NS-OV (a) and the reaction time on the Pd_{0.5}/NS-OV (b) for the selective photocatalytic transformation of BA.

the feature of the solvent molecules. In addition to the above merit, CH₃CN is much more green solvent than others solvents. Therefore, CH₃CN was chosen as a solvent for the photocatalytic reaction.

The stability of photocatalyst is also one of the most important factors to be considered for the development of applicable photocatalytic materials. The stability in the photocatalytic performance and structural stability of Pd_{0.5}/NS-OV for the selective oxidative coupling of BA to form N-benzylidenebenzylamine have been studied under visible light irradiation at 1 atm air pressure. Fig. S12 shows the results of the cycle test of the photocatalytic oxidative coupling of BA on the Pd_{0.5}/NS-OV catalysts. As shown in Fig. S12, the high conversion of BA (>95%) and high selectivity for the formation of N-benzylidenebenzylamine are maintained well even after the reuse of five cycles. ICP-OES confirmed

that the content of Pd on the Pd_{0.5}/NS-OV is practically unchanged before and after reused. The XRD patterns (Fig. S13) also exhibit that the Pd_{0.5}/NS-OV scarcely changes in their crystal structure after the reuse of five cycles.

The photocatalytic performances of the Pd_{0.5}/NS-OV has widely been explored for the selective oxidative coupling of amine derivatives to produce their corresponding imines. The results are listed in Table 2. The Pd_{0.5}/NS-OV catalyst exhibits a high efficiency for the visible light-driven photocatalytic transformation of amines at 1 atm air pressure. As shown in Table 2, entry 2 and 3, the substrates with an electron-withdrawing group are more challenging to oxidize amines into their corresponding imines, particularly, the substrates with a functional group of Cl. The electron inductive effect of an electron-withdrawing

Table 2

Aerobic photocatalytic oxidation of derivatives of different amines on Pd_{0.5}/NS-OV.^a

<chem>Rc1ccc(N)cc1</chem> $\xrightarrow[\lambda \geq 400 \text{ nm, Air}]{\text{Catalyst}}$ <chem>Rc1ccc(N=Cc2ccc(R)cc2)cc1</chem>				
Entry	Substrate	Product	Conv. (%)	Sel. (%)
1	<chem>Nc1ccccc1</chem>	<chem>N=Cc1ccccc1</chem>	95.1	98.2
2	<chem>Nc1ccc(F)cc1</chem>	<chem>N=Cc1ccc(F)cc1</chem>	91.7	99.2
3	<chem>Nc1ccc(Cl)cc1</chem>	<chem>N=Cc1ccc(Cl)cc1</chem>	73.6	99.4
4	<chem>Nc1ccc(C)cc1</chem>	<chem>N=Cc1ccc(C)cc1</chem>	98.9	98.2
5	<chem>Nc1ccc(OC)cc1</chem>	<chem>N=Cc1ccc(OC)cc1</chem>	98.1	99.7
6	<chem>Nc1ccc2c(c1)occc2</chem>	<chem>N=Cc1ccc2c(c1)occc2</chem>	97.4	98.9
7	<chem>Nc1ccc(OC)cc1</chem>	<chem>N=Cc1ccc(OC)cc1</chem>	98.0	99.7

^a Reaction conditions: benzylamine (0.2 mmol), catalyst (10 mg), acetonitrile (1.5 mL), air (1 atm), irradiation time (12 h).

group is found to play an important role in the activation of α -carbon, leading to an enhancement in the oxidative coupling of C-N bonds [52]. Compared with -F group, the group of -Cl exhibits relatively weak electron inductive effect. Therefore, the activation of α -carbon is not enough, leading to a poor conversion of 4-chlorobenzylamine. On the other hand, as shown in Table 2, entries 4–5, the reactant substrates with an electron-donating group exhibit a high efficiency in the same reaction to produce their corresponding imines under the same reaction conditions. These results are attributable to the conjugative effect of the substituent groups. In addition, as shown in Table 2, entries 5–7, the para and meta substitution of the reactant substrates lead to more activation of α -carbon of the reactants to produce the C-N bonds than that of ortho substitution.

3.3. Surface charges transfer enhanced by the Pd sites

The effects of the electronic structure, surface chemistry and interface behaviors of the catalyst on their photocatalytic activities for the selective oxidative coupling of BA were fully investigated on Pd_{0.5}/NS-OV catalyst in aiming to elucidate the intrinsic factors in photocatalysis. The transient photocurrent response and electrochemical impedance spectroscopy (EIS) were measured to investigate the efficiency of the separation of the photo-generated charge carriers in the prepared catalysts. As shown in Fig. 7a, the NS-OV exhibits a higher photocurrent intensity than the Plate catalyst. These results clearly suggest that more successful separation of the photo-generated electron-hole pairs into free electrons and holes as well as their transfer to the surface active sites proceed on NS-OV than that on the Plate catalysts, being attributed to the fact that the surface oxygen vacancies easily induce the charges transfer from bulk to surface as mentioned above [53,54].

Moreover, as shown in Fig. 7a, the efficiency of the separation of photo-generated electron-hole pair is enhanced by the deposition of Pd nanoparticles on the surfaces. As a result, the Pd_{0.5}/NS-OV exhibits the least resistance in the efficiency of the charge migration on the surface. As shown in Fig. 7b, the Pd_{0.5}/NS-OV exhibits the smallest EIS arc radius among NS-OV and Plate catalysts. Similarly, the arc radius of the NS-OV was found to be smaller than that of the Plate. From these results, it is deduced that the surface Pd nanoparticles play an important role in acceleration of charges transfer on the surface of NS-O, promoting the transformation of reactants at interface.

3.4. Surface/Interface coordination activation of BA on the NS-OV

As mentioned above, the oxygen vacancies sites on the surfaces play an important role in the generation of the low coordinated Bi atoms. These exposed metal sites on the surfaces operate also as the strong Lewis acidic sites for the chemically coordinated adsorption [55,56].

Based on the chemical states of the surfaces of the prepared catalysts, the selective adsorption for BA and N-benzylidenebenzylamine has been investigated to understand the transformation processes in the photocatalytic reaction. The adsorption behavior on the interface of BiOCl has been studied by in-situ FTIR measurements. Fig. 8a shows the adsorption of BA molecules on the NS-OV. The NS-OV was firstly degassed at 150 °C under 5 Pa to remove the surface contaminants (Fig. 8a, line (1)). Then, BA was adsorbed for 30 min at room temperature. As shown in Fig. 8a, line (2), the apparent peaks at 1495 and 1454 cm⁻¹ are observed, being assigned to the stretching vibration of the C=C bonds in aromatic ring of BA molecules. The peaks due to the stretching vibration of C-N bonds (ν_{C-N}) of BA are also observed at 1316 cm⁻¹, suggesting that BA molecules adsorb on the surface of the NS-OV. As shown in Fig. 8a, line (3), these peaks are observed even after further heating at 150 °C under vacuum of 5 pa (Fig. 8a, line (3)), confirming that BA molecules strongly adsorb on the surface of the catalyst. As shown in Fig. 8a, line (4), the peak assigned to ν_{C-N} (1316 cm⁻¹) of the adsorbed BA molecules exhibits a little shift to lower wavenumber region in comparison with that of ν_{C-N} (1322 cm⁻¹) of free BA molecules. By considering the presence of the low-coordinated Bi sites on the surface of NS-OV, these results clearly indicate that BA molecules is strongly chemically adsorbed on the surface of NS-OV via the formation of -C-N...Bi coordination bonds at the interface.

The adsorption behavior of BA molecules on the Plate catalyst with poor oxygen vacancies has also been investigated to elucidate the effect of the surface structure on the adsorption behavior of the reactants. As shown in Fig. 8b, the characteristic peaks of BA molecules adsorbed on the Plate exhibit that the adsorption of BA is much weaker than that on the NS-OV, indicating less numbers of the low-coordinated Bi sites on the surface of Plate catalyst. In comparison with the NS-OV catalyst, the Plate exhibits the lower concentration of the oxygen vacancies on the surfaces, which resulting in a decrease in the number of the unsaturated Bi sites on the surfaces.

In order to clarify the precise selectivity for the formation of N-benzylidenebenzylamine, the adsorption of N-benzylidenebenzylamine molecules on the NS-OV catalyst has been studied. As shown in Fig. 8c and d, the characteristic peaks due to N-benzylidenebenzylamine molecules unable to observe after adsorption on NS-OV and Plate, suggesting that both NS-OV and Plate unable to adsorb or capture N-benzylidenebenzylamine molecules. These results clearly indicates that the specific adsorption of BA molecules on the low-coordinated Bi sites on NS-OV catalyst is very important not only for the transformation of BA to form the desired its corresponding imine product but also for the maintenance of adsorption cycles of BA molecules. These ideal circumstances the NS-OV catalyst lead to the high photocatalytic conversion of BA and high selectivity for the formation of N-benzylidenebenzylamine with an assistance of Pd nanoparticles as a co-

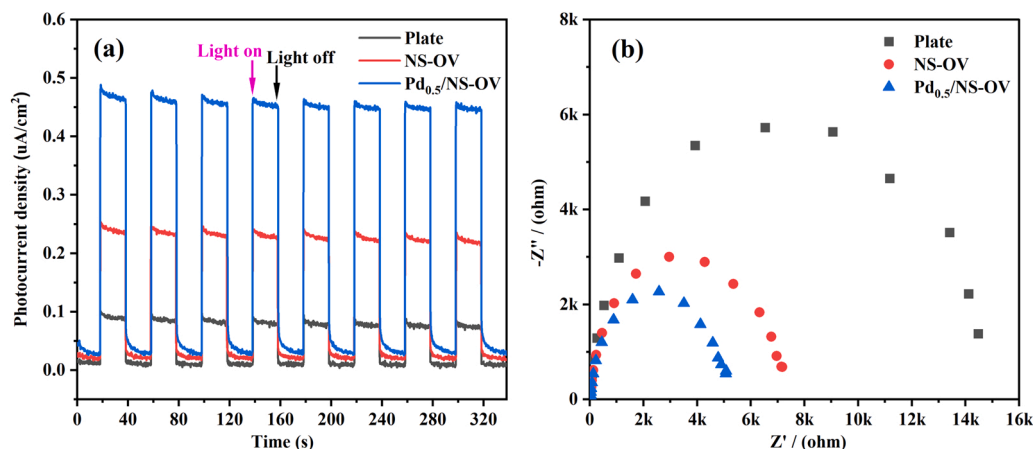


Fig. 7. (a) The response of the transient photocurrent for the prepared catalysts and (b) EIS Nyquist plots.

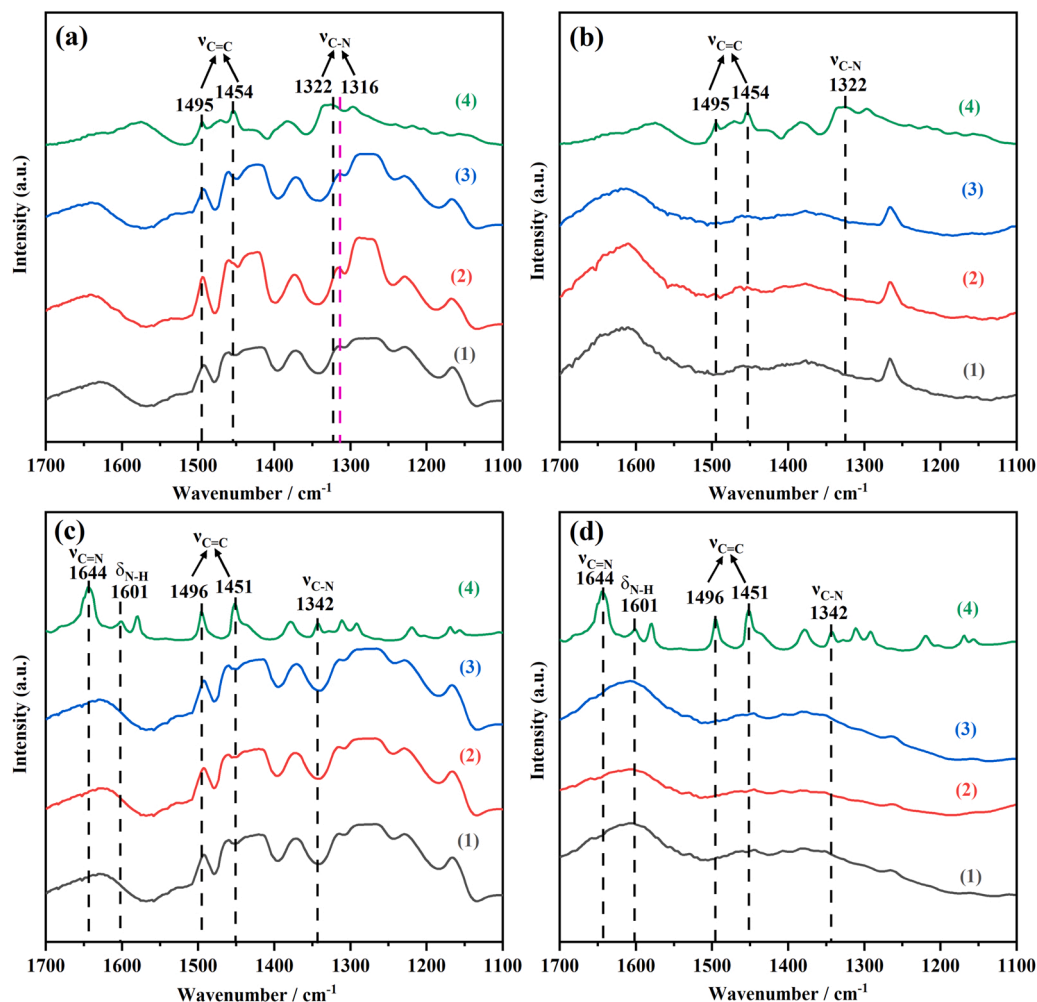


Fig. 8. In situ FTIR spectra of (a) NS-OV, (b) Plate for BA adsorption, (c) NS-OV and (d) Plate for N-benzylidenebenzylamine adsorption. (1) After degassing at 150 °C for 3 h. (2) Adsorption for 30 min at room temperature (physical adsorption + chemical adsorption). (3) Further evacuation of the excess BA/N-benzylidenebenzylamine at 150 °C for 15 min under 5×10^{-2} hPa (chemical adsorption). (4) FTIR spectra of BA/N-benzylidenebenzylamine supported on KBr.

catalyst.

3.5. Assembling and activating of O_2 on OV sites

The next issue to be solved is how do O_2 molecules participate in the photocatalytic oxidation of BA. EPR measurements has been carried out to study the role of oxygen species as active intermediates. As shown in Fig. 9(a), obvious EPR signals unable to observe for the pure NS-OV and

$Pd_{0.5}/NS-OV$ catalysts under dark conditions. On the other hand, obvious EPR signals assigned to $\cdot O_2^-$ anion radical are observed for the pure NS-OV catalyst under visible light irradiation by applying DMPO as a radical scavenger [32,52]. These results clearly indicated that the irradiation of the catalyst with visible light induced the formation of $\cdot O_2^-$ anion radicals by reducing O_2 with a photo-generated electrons. As aforementioned, Pd nanoparticles improve the transfer of photo-generated electrons, in fact, as shown in Fig. 9a, the EPR signals

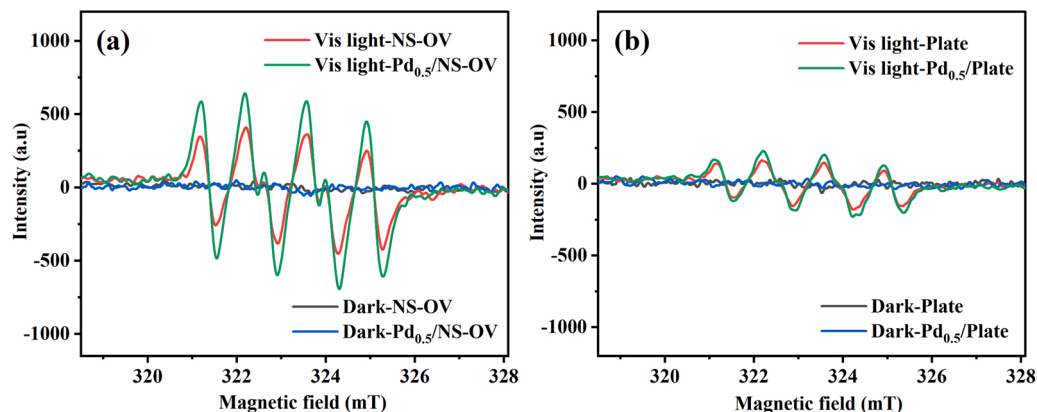


Fig. 9. EPR spectra (a) NS-OV and $Pd_{0.5}/NS-OV$, (b) Plate and $Pd_{0.5}/Plate$.

due to $\bullet\text{O}_2^-$ anion radicals are greatly enhanced in the intensity on the $\text{Pd}_{0.5}/\text{NS-OV}$, showing the formation of much higher concentration of $\bullet\text{O}_2^-$ anion radicals on the $\text{Pd}_{0.5}/\text{NS-OV}$ catalyst. These results clearly suggest that O_2 molecules are activated to $\bullet\text{O}_2^-$ anion radicals and operate as an oxidant for the formation of -C-N- oxidative coupling in the reaction.

For the further investigation on the roles of oxygen vacancies in the generation of $\bullet\text{O}_2^-$ anion radicals, EPR signals on the Plate catalysts were measured. As shown in Fig. 9b, both Plate and $\text{Pd}_{0.5}/\text{Plate}$ catalysts unable to produce the $\bullet\text{O}_2^-$ anion radicals without the irradiation of visible light. As shown in Fig. 9, under visible light irradiation, both Plate and $\text{Pd}_{0.5}/\text{Plate}$ catalysts exhibit obvious EPR signals due to $\bullet\text{O}_2^-$ anion radicals [52]. In comparison with the NS-OV, the Plate exhibited very weak signals due to $\bullet\text{O}_2^-$ anion radicals, suggesting that the oxygen vacancies on the surfaces operate to promote assembling of O_2 molecules onto the surface of photocatalyst. Furthermore, as mentioned above, Pd nanoparticles work to accelerate the reduction of O_2 molecules to form $\bullet\text{O}_2^-$ anion radicals. As a result, the $\text{Pd}_{0.5}/\text{NS-OV}$ catalyst exhibits much higher efficiency for the photocatalytic oxidative coupling of BA than $\text{Pd}_{0.5}/\text{Plate}$. Based on these results, it is deduced that the oxygen vacancies and the low-coordinated Bi sites on the surfaces play an important role in the photocatalytic transformation of BA with cooperation of Pd nanoparticles as co-catalyst.

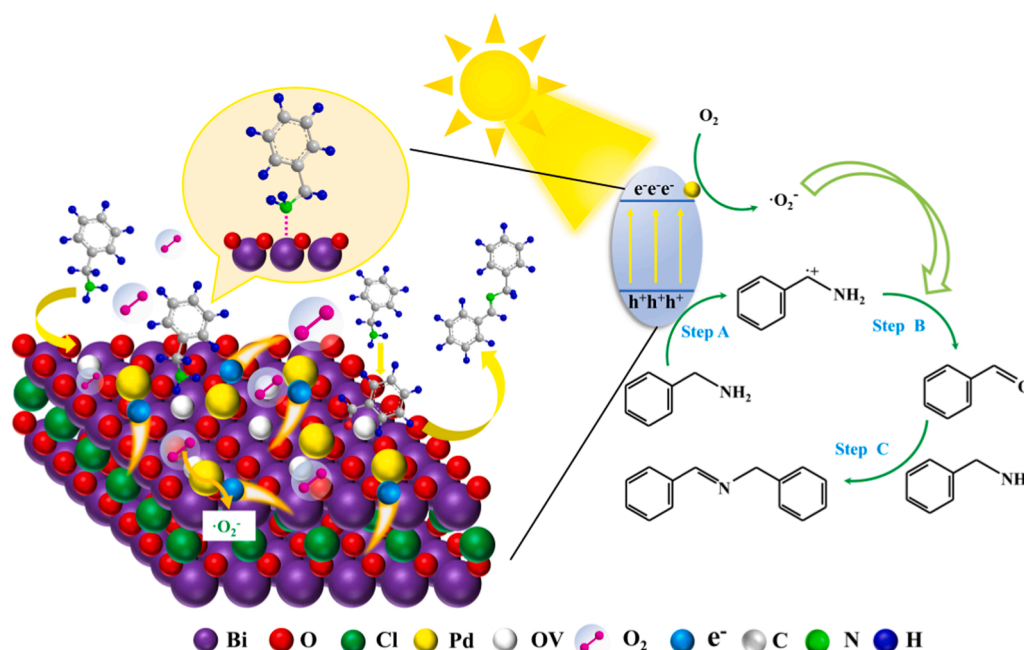
3.6. Mechanism of precisely photocatalytic BA coupling to N-benzylidenebenzylamine

On the basis of aforementioned results and discussions, a possible photocatalytic reaction mechanism for the selective oxidative coupling of benzylamines (BA) to N-benzylidenebenzylamine on the $\text{Pd}_{0.5}/\text{NS-OV}$ catalyst is proposed. As shown in Scheme 1, BA molecules strongly chemically adsorbed on the low-coordinated Bi sites on the surfaces through the formation of the -N...Bi- coordination bonds at the interfaces. The formation of -N...Bi- coordination bonds induces the polarization in -C-N bonds in BA molecules (Step A), resulting in the activation of α -carbon of BA. At the same time, the surface OV sites assemble O_2 molecules on the surfaces. Under visible light irradiation, electrons and holes are generated in the NS-OV catalyst. The transfer of electrons to the surface of the NS-OV is improved by the presence of Pd

nanoparticles, which also play an important role in the further reduction of adsorbed O_2 molecules to produce active $\bullet\text{O}_2^-$ anion radicals. On the other hand, the photo-formed holes operate to strengthen the polarization and activation of -C-N- bonds of adsorbed BA molecules by inducing the charge transfer from -N- moiety of BA to low-coordinated Bi site through the -N...Bi- coordination bonds. As a result, the activation of -C-N...Bi- coordination complexes by $\bullet\text{O}_2^-$ anion radicals is promoted to form intermediate species of Ar-CH=O (Step B). The intermediate species of Ar-CH=O easily integrate with free BA molecules (Step C) to form the desired corresponding final product of N-benzylidenebenzylamine. Once formed N-benzylidenebenzylamine is not over-oxidized since it did not adsorb on the NS-OV catalyst. Thus, the synergetic effects of the oxygen vacancies, low-coordinated Bi sites and Pd nanoparticles on the surfaces make possible that the $\text{Pd}_{0.5}/\text{NS-OV}$ operates as a highly efficient photocatalyst for the oxidative coupling transformation of BA to N-benzylidenebenzylamine with a high selectivity under visible light irradiation at 1 atm air pressure and room temperature.

4. Conclusion

The ultrathin BiOCl nanosheets with two atom layers thickness were successfully prepared via the one step solvothermal method. The characteristic structures of the ultrathin nanosheet resulted in the formation of abundant oxygen vacancies and low-coordinated Bi sites on the surface of the nanosheets (NS-OV) catalyst. The detailed analyses on the chemical states of the surfaces of NS-OV catalyst enable to induce a multi-functional photocatalytic reaction mechanism for the selective oxidative coupling of benzylamine to form N-benzylidenebenzylamine, which proceeding on $\text{Pd}_{0.5}/\text{NS-OV}$ (Pd: 0.5 wt%) catalyst under visible light irradiation at 1 atm air pressure and room temperature. BA molecules adsorbed strongly on the low-coordinated Bi sites on the surfaces through the formation of the -N...Bi- coordination bonds at interfaces, which inducing the polarization of the -C-N bonds of BA molecules. Moreover, the oxygen vacancies on the surfaces operate as the active sites to assemble O_2 molecules on the surfaces. Under visible light irradiation, the photo-generated electrons of the catalyst enable to reduce the adsorbed O_2 to form $\bullet\text{O}_2^-$ anion radicals. On the other hand, the photo-generated holes operate to promote the charge transfer from the -N- moiety of BA to the low-coordinated Bi sites through the formed



Scheme 1. Proposed mechanism for the photocatalytic selective oxidative coupling of BA on $\text{Pd}_{0.5}/\text{NS-OV}$ catalyst under visible light irradiation.

N•••Bi- coordination bonds. The Pd nanoparticles on the surfaces operate to enhance the migration of photo-formed electrons from inside to surface of catalyst, which results in an acceleration of the reduction of O₂ molecules to form O₂^{•-} anion radicals. As a result, the Pd_{0.5}/NS-OV photocatalyst exhibited the high photocatalytic conversion of benzylamine (>95%) to produce desired corresponding product of N-benzylidenebenzylamine with a high selectivity (>98%). Thus, the synergistic effects of the oxygen vacancies, the low-coordinated Bi sites and Pd nanoparticles on the surfaces play important roles in the photocatalytic precise transformation of BA to N-benzylidenebenzylamine.

CRedit authorship contribution statement

Shuai Wei: Conceptualization, Investigation, Formal analysis. **Hongxiao Zhong:** Formal analysis, Experimental measurements. **Hongtao Wang:** Date curation. **Yujie Song:** Conceptualization, Writing – review & editing. **Chunman Jia:** Test assistance. **Masakazu Anpo:** Writing – review & editing. **Ling Wu:** Writing – review & editing.

Declaration of Competing Interest

The authors declare that they have no known competing financial interests or personal relationships that could have appeared to influence the work reported in this paper.

Acknowledgments

This work was supported by the National Natural Science Foundation of China (22002030 and 51672048), The assistance of Dr. Binbin Guo for the measurements of XPS is highly appreciated.

Appendix A. Supporting information

Supplementary data associated with this article can be found in the online version at [doi:10.1016/j.apcatb.2021.121032](https://doi.org/10.1016/j.apcatb.2021.121032).

References

- [1] C. Yang, B. Wang, L. Zhang, L. Yin, X. Wang, Synthesis of layered carbonitrides from biotic molecules for photoredox transformations, *Angew. Chem. Int. Ed.* 56 (2017) 6627–6631.
- [2] C. Xing, G. Yu, T. Chen, S. Liu, Q. Sun, Q. Liu, Y. Hu, H. Liu, X. Li, Perylenetetracarboxylic diimide covalently bonded with mesoporous g-C₃N₄ to construct direct Z-scheme heterojunctions for efficient photocatalytic oxidative coupling of amines, *Appl. Catal. B: Environ.* 298 (2021), 120534.
- [3] Y.-X. Tan, Z.-M. Chai, B.-H. Wang, S. Tian, X.-X. Deng, Z.-J. Bai, L. Chen, S. Shen, J.-K. Guo, M.-Q. Cai, C.-T. Au, S.-F. Yin, Boosted photocatalytic oxidation of toluene into benzaldehyde on CdIn₂S₄-CdS: synergistic effect of compact heterojunction and S-vacancy, *ACS Catal.* 11 (2021) 2492–2503.
- [4] H. Liu, C. Xu, D. Li, H.-L. Jiang, Photocatalytic hydrogen production coupled with selective benzylamine oxidation over MOF, *Compos., Angew. Chem. Int. Ed.* 57 (2018) 5379–5383.
- [5] T. Wang, X. Tao, X. Li, K. Zhang, S. Liu, B. Li, Synergistic Pd single atoms, clusters, and oxygen vacancies on TiO₂ for photocatalytic hydrogen evolution coupled with selective organic oxidation, *Small* 17 (2021) 2006255.
- [6] H. Xu, X. Li, H. Hao, X. Dong, W. Sheng, X. Lang, Designing fluorene-based conjugated microporous polymers for blue light-driven photocatalytic selective oxidation of amines with oxygen, *Appl. Catal. B: Environ.* 285 (2021), 119796.
- [7] B. Yuan, R. Chong, B. Zhang, J. Li, Y. Liu, C. Li, Photocatalytic aerobic oxidation of amines to imines on BiVO₄ under visible light irradiation, *Chem. Commun.* 50 (2014) 15593–15596.
- [8] N. Zhang, X. Li, H. Ye, S. Chen, H. Ju, D. Liu, Y. Lin, W. Ye, C. Wang, Q. Xu, J. Zhu, L. Song, J. Jiang, Y. Xiong, Oxide Defect Engineering Enables to Couple Solar Energy into Oxygen Activation, *J. Am. Chem. Soc.* 138 (2016) 8928–8935.
- [9] Q. Xiao, T.U. Connell, J.J. Cadusch, A. Roberts, A.S.R. Chesman, D.E. Gómez, Hot-carrier organic synthesis via the near-perfect absorption of light, *ACS Catal.* 8 (2018) 10331–10339.
- [10] Y. Xiao, G. Tian, W. Li, Y. Xie, B. Jiang, C. Tian, D. Zhao, H. Fu, Molecule self-assembly synthesis of porous few-layer carbon nitride for highly efficient photoredox catalysis, *J. Am. Chem. Soc.* 141 (2019) 2508–2515.
- [11] W. Zou, X.-H. Liu, C. Xue, X.-T. Zhou, H.-Y. Yu, P. Fan, H.-B. Ji, Enhancement of the visible-light absorption and charge mobility in a zinc porphyrin polymer/g-C₃N₄ heterojunction for promoting the oxidative coupling of amines, *Appl. Catal. B: Environ.* 285 (2021), 119863.
- [12] Z.J. Wang, S. Ghasimi, K. Landfester, K.A.I. Zhang, Molecular structural design of conjugated microporous poly(benzoxadiazole) networks for enhanced photocatalytic activity with visible light, *Adv. Mater.* 27 (2015) 6265–6270.
- [13] Y. Zhi, K. Li, H. Xia, M. Xue, Y. Mu, X. Liu, Robust porous organic polymers as efficient heterogeneous organo-photocatalysts for aerobic oxidation reactions, *J. Mater. Chem. A* 5 (2017) 8697–8704.
- [14] D. Sun, L. Ye, Z. Li, Visible-light-assisted aerobic photocatalytic oxidation of amines to imines over NH₂-MIL-125(Ti), *Appl. Catal. B: Environ.* 164 (2015) 428–432.
- [15] Y. Zhang, J. Pang, J. Li, X. Yang, M. Feng, P. Cai, H.-C. Zhou, Visible-light harvesting pyrene-based MOFs as efficient ROS generators, *Chem. Sci.* 10 (2019) 8455–8460.
- [16] J. Chen, J. Xiong, Y. Song, Y. Yu, L. Wu, Synthesis of nitrosobenzene via photocatalytic oxidation of aniline over MgO/TiO₂ under visible light irradiation, *Appl. Surf. Sci.* 440 (2018) 1269–1276.
- [17] M.-Y. Qi, M. Conte, M. Anpo, Z.-R. Tang, Y.-J. Xu, Cooperative coupling of oxidative organic synthesis and hydrogen production over semiconductor-based photocatalysts, *Chem. Rev.* (2021).
- [18] X. Bao, H. Li, Z. Wang, F. Tong, M. Liu, Z. Zheng, P. Wang, H. Cheng, Y. Liu, Y. Dai, Y. Fan, Z. Li, B. Huang, TiO₂/Ti₃C₂ as an efficient photocatalyst for selective oxidation of benzyl alcohol to benzaldehyde, *Appl. Catal. B: Environ.* 286 (2021), 119885.
- [19] Z. Zhou, Y.-N. Xie, W. Zhu, H. Zhao, N. Yang, G. Zhao, Selective photoelectrocatalytic tuning of benzyl alcohol to benzaldehyde for enhanced hydrogen production, *Appl. Catal. B: Environ.* 286 (2021), 119868.
- [20] K. Jing, J. Xiong, N. Qin, Y. Song, L. Li, Y. Yu, S. Liang, L. Wu, Development and photocatalytic mechanism of monolayer Bi₂MoO₆ nanosheets for the selective oxidation of benzylic alcohols, *Chem. Commun.* 53 (2017) 8604–8607.
- [21] Y. Song, H. Wang, Z. Wang, B. Guo, K. Jing, Y. Li, L. Wu, Selective photocatalytic synthesis of haloanilines from halonitrobenzenes over multifunctional AuPt/monolayer titanate nanosheet, *ACS Catal.* 8 (2018) 9656–9664.
- [22] Y. Song, H. Wang, G. Liu, H. Wang, L. Li, Y. Yu, L. Wu, Constructing surface synergistic effect in Cu-Cu₂O hybrids and monolayer H_{1.4}Ti_{1.65}O₄·H₂O nanosheets for selective cinnamyl alcohol oxidation to cinnamaldehyde, *J. Catal.* 370 (2019) 461–469.
- [23] X. Li, Y. Sun, J. Xu, Y. Shao, J. Wu, X. Xu, Y. Pan, H. Ju, J. Zhu, Y. Xie, Selective visible-light-driven photocatalytic CO₂ reduction to CH₄ mediated by atomically thin CuIn₂S₃ layers, *Nat. Energy* 4 (2019) 690–699.
- [24] J. Zou, Z. Wang, W. Guo, B. Guo, Y. Yu, L. Wu, Photocatalytic selective oxidation of benzyl alcohol over ZnTi-LDH: The effect of surface OH groups, *Appl. Catal. B: Environ.* 260 (2020), 118185.
- [25] X. Li, L. Liang, Y. Sun, J. Xu, X. Jiao, X. Xu, H. Ju, Y. Pan, J. Zhu, Y. Xie, Ultrathin conductor enabling efficient IR light CO₂ reduction, *J. Am. Chem. Soc.* 141 (2019) 423–430.
- [26] J.-L. Shi, R. Chen, H. Hao, C. Wang, X. Lang, 2D sp² carbon-conjugated porphyrin covalent organic framework for cooperative photocatalysis with TEMPO, *Angew. Chem. Int. Ed.* 59 (2020) 9088–9093.
- [27] J. Jiang, K. Zhao, X. Xiao, L. Zhang, Synthesis and facet-dependent photoreactivity of BiOCl single-crystalline nanosheets, *J. Am. Chem. Soc.* 134 (2012) 4473–4476.
- [28] H. Li, J. Shang, J. Shi, K. Zhao, L. Zhang, Facet-dependent solar ammonia synthesis of BiOCl nanosheets via a proton-assisted electron transfer pathway, *Nanoscale* 8 (2016) 1986–1993.
- [29] W. Ouyang, F. Teng, X. Fang, High performance BiOCl nanosheets/TiO₂ nanotube arrays heterojunction UV photodetector: the influences of self-induced inner electric fields in the BiOCl nanosheets, *Adv. Funct. Mater.* 28 (2018) 1707178.
- [30] M. Guan, C. Xiao, J. Zhang, S. Fan, R. An, Q. Cheng, J. Xie, M. Zhou, B. Ye, Y. Xie, Vacancy associates promoting solar-driven photocatalytic activity of ultrathin bismuth oxychloride nanosheets, *J. Am. Chem. Soc.* 135 (2013) 10411–10417.
- [31] H. Li, J. Li, Z. Ai, F. Jia, L. Zhang, Oxygen vacancy-mediated photocatalysis of BiOCl: reactivity, selectivity, and perspectives, *Angew. Chem. Int. Ed.* 57 (2018) 122–138.
- [32] H. Li, F. Qin, Z. Yang, X. Cui, J. Wang, L. Zhang, New reaction pathway induced by plasmon for selective benzyl alcohol oxidation on BiOCl possessing oxygen vacancies, *J. Am. Chem. Soc.* 139 (2017) 3513–3521.
- [33] Y. Ren, J. Zou, K. Jing, Y. Liu, B. Guo, Y. Song, Y. Yu, L. Wu, Photocatalytic synthesis of N-benzylamine from benzylamine on ultrathin BiOCl nanosheets under visible light, *J. Catal.* 380 (2019) 123–131.
- [34] H. Li, L. Zhang, Oxygen vacancy induced selective silver deposition on the {001} facets of BiOCl single-crystalline nanosheets for enhanced Cr(VI) and sodium pentachlorophenate removal under visible light, *Nanoscale* 6 (2014) 7805–7810.
- [35] R. Shi, Y. Zhao, G.I.N. Waterhouse, S. Zhang, T. Zhang, Defect engineering in photocatalytic nitrogen fixation, *ACS Catal.* 9 (2019) 9739–9750.
- [36] H. Li, J. Shi, K. Zhao, L. Zhang, Sustainable molecular oxygen activation with oxygen vacancies on the {001} facets of BiOCl nanosheets under solar light, *Nanoscale* 6 (2014) 14168–14173.
- [37] Z. Wang, H. Wang, X. Wang, X. Chen, Y. Yu, W. Dai, X. Fu, M. Anpo, Correlation between photocorrosion of ZnO and lattice relaxation induced by its surface vacancies, *J. Phys. Chem. C* 125 (2021) 3242–3255.
- [38] H. Chen, L. Peng, Y. Bian, X. Shen, J. Li, H.-C. Yao, S.-Q. Zang, Z. Li, Exerting charge transfer to stabilize Au nanoclusters for enhanced photocatalytic performance toward selective oxidation of amines, *Appl. Catal. B: Environ.* 284 (2021), 119704.
- [39] T. Wang, X. Tao, Y. Xiao, G. Qiu, Y. Yang, B. Li, Charge separation and molecule activation promoted by Pd/MIL-125-NH₂ hybrid structures for selective oxidation reactions, *Catal. Sci. Technol.* 10 (2020) 138–146.

- [40] J. Liu, S. Zhang, H. Zhao, Fabricating visible-light photoactive 3D flower-like BiOCl nanostructures via a one-step solution chemistry method at room temperature, *Appl. Surf. Sci.* 479 (2019) 247–252.
- [41] Z. Sun, X. Yang, X.-F. Yu, L. Xia, Y. Peng, Z. Li, Y. Zhang, J. Cheng, K. Zhang, J. Yu, Surface oxygen vacancies of Pd/Bi₂MoO_{6-x} acts as “Electron Bridge” to promote photocatalytic selective oxidation of alcohol, *Appl. Catal. B: Environ.* 285 (2021), 119790.
- [42] S. Bai, X. Li, Q. Kong, R. Long, C. Wang, J. Jiang, Y. Xiong, Toward enhanced photocatalytic oxygen evolution: synergetic utilization of plasmonic effect and schottky junction via interfacing facet selection, *Adv. Mater.* 27 (2015) 3444–3452.
- [43] X. Li, T. Wang, X. Tao, G. Qiu, C. Li, B. Li, Interfacial synergy of Pd sites and defective BiOBr for promoting the solar-driven selective oxidation of toluene, *J. Mater. Chem. A* 8 (2020) 17657–17669.
- [44] J. Cao, J. Li, W. Chu, W. Cen, Facile synthesis of Mn-doped BiOCl for metronidazole photodegradation: Optimization, degradation pathway, and mechanism, *Chem. Eng. J.* 400 (2020), 125813.
- [45] Y. Zheng, T. Zhou, X. Zhao, W.K. Pang, H. Gao, S. Li, Z. Zhou, H. Liu, Z. Guo, Atomic interface engineering and electric-field effect in ultrathin Bi₂MoO₆ nanosheets for superior lithium ion storage, *Adv. Mater.* 29 (2017) 1700396.
- [46] Z.-W. Wang, Q. Wan, Y.-Z. Shi, H. Wang, Y.-Y. Kang, S.-Y. Zhu, S. Lin, L. Wu, Selective photocatalytic reduction CO₂ to CH₄ on ultrathin TiO₂ nanosheet via coordination activation, *Appl. Catal. B: Environ.* 288 (2021), 120000.
- [47] J. Wan, W. Chen, C. Jia, L. Zheng, J. Dong, X. Zheng, Y. Wang, W. Yan, C. Chen, Q. Peng, D. Wang, Y. Li, Defect effects on TiO₂ nanosheets: stabilizing single atomic site Au and promoting catalytic properties, *Adv. Mater.* 30 (2018) 1705369.
- [48] S. Gao, B. Gu, X. Jiao, Y. Sun, X. Zu, F. Yang, W. Zhu, C. Wang, Z. Feng, B. Ye, Y. Xie, Highly efficient and exceptionally durable CO₂ photoreduction to methanol over freestanding defective single-unit-cell bismuth vanadate layers, *J. Am. Chem. Soc.* 139 (2017) 3438–3445.
- [49] Y. Lv, W. Yao, R. Zong, Y. Zhu, Fabrication of wide-range-visible photocatalyst Bi₂WO_{6x} nanoplates via surface oxygen vacancies, *Sci. Rep.* 6 (2016) 19347.
- [50] S. Sarina, H.-Y. Zhu, Q. Xiao, E. Jaatinen, J. Jia, Y. Huang, Z. Zheng, H. Wu, Viable photocatalysts under solar-spectrum irradiation: nonplasmonic metal nanoparticles, *Angew. Chem. Int. Ed.* 53 (2014) 2935–2940.
- [51] M. Anpo, G. Costentin, E. Giamello, H. Lauron-Pernot, Z. Sojka, Characterisation and reactivity of oxygen species at the surface of metal oxides, *J. Catal.* 393 (2021) 259–280.
- [52] H. Wang, D. Yong, S. Chen, S. Jiang, X. Zhang, W. Shao, Q. Zhang, W. Yan, B. Pan, Y. Xie, Oxygen-vacancy-mediated exciton dissociation in BiOBr for boosting charge-carrier-involved molecular oxygen activation, *J. Am. Chem. Soc.* 140 (2018) 1760–1766.
- [53] H.L. Tan, F.F. Abdi, Y.H. Ng, Heterogeneous photocatalysts: an overview of classic and modern approaches for optical, electronic, and charge dynamics evaluation, *Chem. Soc. Rev.* 48 (2019) 1255–1271.
- [54] H. Wu, H.L. Tan, C.Y. Toe, J. Scott, L. Wang, R. Amal, Y.H. Ng, Photocatalytic and Photoelectrochemical Systems: Similarities and Differences, *Adv. Mater.* 32 (2020) 1904717.
- [55] R. Guan, D. Wang, Y. Zhang, C. Liu, W. Xu, J. Wang, Z. Zhao, M. Feng, Q. Shang, Z. Sun, Enhanced photocatalytic N₂ fixation via defective and fluoride modified TiO₂ surface, *Appl. Catal. B: Environ.* 282 (2021), 119580.
- [56] C. Liang, H.-Y. Niu, H. Guo, C.-G. Niu, Y.-Y. Yang, H.-Y. Liu, W.-W. Tang, H.-P. Feng, Efficient photocatalytic nitrogen fixation to ammonia over bismuth monoxide quantum dots-modified defective ultrathin graphitic carbon nitride, *Chem. Eng. J.* 406 (2021), 126868.